

# FID modulus: a simple and efficient technique to phase and align MR spectra

Yann Le Fur · Patrick J. Cozzone

Received: 25 February 2013 / Revised: 13 May 2013 / Accepted: 14 May 2013 / Published online: 21 June 2013  
© ESMRMB 2013

## Abstract

**Object** The post-processing of MR spectroscopic data requires several steps more or less easy to automate, including the phase correction and the chemical shift assignment. First, since the absolute phase is unknown, one of the difficulties the MR spectroscopist has to face is the determination of the correct phase correction. When only a few spectra have to be processed, this is usually performed manually. However, this correction needs to be automated as soon as a large number of spectra is involved, like in the case of phase coherent averaging or when the signals collected with phased array coils have to be combined. A second post-processing requirement is the frequency axis assignment. In standard mono-voxel MR spectroscopy, this can also be easily performed manually, by simply assigning a frequency value to a well-known resonance (e.g. the water or NAA resonance in the case of brain spectroscopy). However, when the correction of a frequency shift is required before averaging a large amount of spectra (due to  $B_0$  spatial inhomogeneities in chemical shift imaging, or resulting from motion for example), this post-processing definitely needs to be performed automatically.

**Materials and methods** Zero-order phase and frequency shift of a MR spectrum are linked respectively to zero-order and first-order phase variations in the corresponding free induction decay (FID) signal. One of the simplest ways to remove the phase component of a signal is to calculate

the modulus of this signal: this approach is the basis of the correction technique presented here.

**Results** We show that selecting the modulus of the FID allows, under certain conditions that are detailed, to automatically phase correct and frequency align the spectra. This correction technique can be for example applied to the summation of signals acquired from combined phased array coils, to phase coherent averaging and to  $B_0$  shift correction.

**Conclusion** We demonstrate that working on the modulus of the FID signal is a simple and efficient way to both phase correct and frequency align MR spectra automatically. This approach is particularly well suited to brain proton MR spectroscopy.

**Keywords** MR spectroscopy · Free induction decay · Modulus · Post-processing · Phase correction · Frequency assignment

## Abbreviations

Composite signal	A simulated signal composed of one or several FIDs, and eventually a noise signal
Conventional processing	Refers to the conventional post-processing performed on the original FID signal: this is the conventional technique, compared in this study to the modulus post-processing (see below)
CSI	Chemical shift imaging
FID	Free induction decay
FWHM	Full Width at Half the Maximum
LB	Line broadening in Hz. LB is the full width at half maximum (FWHM) of the peak obtained

Y. Le Fur (✉) · P. J. Cozzone  
Aix-Marseille Université, CNRS, CRMBM UMR 7339,  
13385 Marseille, France  
e-mail: yann.le-fur@univ-amu.fr

P. J. Cozzone  
APHM, Hôpitaux de la Timone, CEMEREM,  
13385 Marseille, France

	after fast Fourier transformation of a time decaying exponential function $e^{(-\pi LBt)}$ [1]
Modulus processing	Refers to the post-processing performed on the modulus of the FID signal as presented in this study and compared to the conventional technique (see above)
MRS	Magnetic resonance spectroscopy
MRI	Magnetic resonance imaging
SNR	Signal-to-noise ratio, calculated as the maximum of the peak over the standard deviation of the noise in a frequency range selected in a region of the spectrum devoid of other signals and/or artifacts
SD	Standard deviation
SW	Spectral width

## Introduction

The interest to combine magnetic resonance spectroscopy (MRS) with magnetic resonance imaging (MRI) in order to improve the diagnosis of brain pathologies in adults and children has been widely demonstrated. Despite the clear added value of MRS, this technique is still not routinely included in clinical examinations. One of the reasons of this limitation is the complexity of the post-processing involved, which cannot be easily automated. This issue is even more challenging in the case of chemical shift imaging (CSI). Most of the spectroscopic processing tools do not allow to perform a reliable phase correction and an accurate frequency shift assignment. In most cases, this can only be performed manually. This process is often slow and it requires an extended theoretical knowledge of spectroscopy. This situation constitutes a deterrent and a source of confusion for radiologists, who are by now extremely familiar and proficient with MRI but still poorly acquainted with MRS techniques and more particularly with CSI, with the exception of single voxel brain spectroscopy which is currently fully automated on modern MR scanners.

Phasing a spectrum is a crucial step when designing an automated fitting procedure, because the knowledge of the phase can be used as prior knowledge for the fitting algorithm and hence decreases the number of parameters to be estimated, thus reducing the risk of fitting errors. When a large number of spectra needs to be phased, as in the case of phase coherent averaging [2], or more recently with the increased usage of phased array coils, the phase correction definitely needs to be automated.

Phased array coils provide a significant improvement in signal-to-noise ratio (SNR) in comparison to standard coil technology. However combining the signals received from all individual coils is not trivial since these signals need to be phased and scaled in order to correct for phase shift and amplification factor respectively and both parameters differ from one coil to another. The phase alignment is also crucial for sensitivity-encoded (SENSE) CSI [3]. Several automatic phase correction schemes have been proposed. They are all based on the use of a signal of reference, usually the water peak, obtained either by repeating the experiment without water saturation, or by applying only a moderate water saturation which keeps enough water signal in the spectrum to be detected and used as a reference. The phase of the reference peak can be obtained by fitting procedures (namely LC-Model [4] but also QUEST [5] or AMARES [6] methods), by calculating the phase of the first point of the FID [7, 8], the phase of the water peak [9, 10], by maximizing the area of a selected resonance [11], or the phase of reference images [12]. Freely available software devoted to post-processing of spectroscopic data also provide an automatic phase correction. Different strategies are used: jMRUI (<http://www.mruui.uab.es/mruui/>) uses the GABOR technique [13], TARQUIN (<http://tarquin.sourceforge.net/>) is based on the minimization of the difference between the spectra and a reference spectrum, jSIPRO (<https://www.sites.google.com/site/jsiprotool/>) exploits the phase of the first point of the FID, Vespa (<http://scion.duhs.duke.edu/vespa/>) proposes either a correlation or an integration method. All these different software and also AQSES (<http://homes.esat.kuleuven.be/~biomed/software.php>) include eddy currents correction, whenever an extra non-suppressed water reference scan is available. MIDAS (<http://mrir.med.miami.edu:8000/midas/wiki>) is strongly linked to the EPSI pulse program sequences [14] and uses a water reference scan acquired in an interleaved way.

Concerning the frequency shift correction, the rationale and arguments justifying the benefits of an accurate phase correction remain valid. Again, the knowledge of the frequency shift can be directly used as prior knowledge for automatic fitting procedures. It can also be exploited in order to increase drastically the number of constraints on this parameter, by reducing the spectral range explored by the fitting procedure. The risk of erroneous attribution of resonances by the fitting algorithm is then reduced. Frequency shift correction definitely needs to be automated when motion effects are present as in the case of phase coherent averaging [2] or J-difference editing [15–17], or when spatial  $B_0$  inhomogeneities need to be compensated in CSI experiments. Several techniques have been proposed to solve these issues and we have already

addressed this topic and proposed solutions in a previous publication [18].

In this paper, we aim to demonstrate that working on the modulus of the FID signal allows to correct simply and automatically for both phase distortions and frequency shifts. This technique assumes that the FID signal is including a reference signal much higher in amplitude than those of the metabolites of interest. In proton MR spectroscopy, this reference signal will naturally be the water resonance. This higher signal can be seen as a “carrier” onto which the metabolites are superimposed. Extracting the modulus of this carrier is equivalent to remove zero- and first-order phase information of this signal, which means that the signal is hence correctly phased and on-resonance. If the amplitudes of the metabolites signals superimposed to the carrier are low enough, they will not be modified by the modulus extraction and they will follow the phase and frequency shift of the carrier. Therefore, they will be themselves phased and shifted, respectively to the carrier. As shown in the present study, the SNR can be either substantially improved or, in the worst case, only slightly decreased.

It has to be noted that Serrai et al. [19] have already proposed the idea of working on the modulus of the FID signal, with the objective of removing the sidebands in non water-suppressed proton spectra. In their study, the spectrum was assumed to be correctly phased and on-resonance, but they did not study what would be the consequences if these two conditions were not fulfilled. As mentioned above, the technique proposed here requires that the FID signal contains a strong reference signal. Therefore the fact that working on the modulus of the FID removes the sidebands created by this strong signal in the resulting spectrum constitutes of course an additional benefit to the approach that we propose.

## Materials and methods

### Signal considerations

Let  $A(t)$  be the signal acquired from a voxel containing a unique compound. If the NMR signal of this compound is a singlet, then the noise-free signal  $A(t)$  can be expressed as:

$$A(t) = A_0(t)e^{j(\omega t + \varphi)} \quad (1)$$

where  $A_0(t)$  is the waveform of the FID,  $\omega$  the resonance frequency of the singlet and  $\varphi$  includes all the phase distortions. A possible way to correct for phase distortion is to consider the modulus of the signal:

$$\|A(t)\| = A_0(t) \quad (2)$$

Considering that the modulus of the signal also removes the frequency information, this results, after fast Fourier transformation, in an “on-resonance” signal. Let’s now assume that this singlet is the water peak. Using the notation already used in Eq. (1), the water signal can be expressed as:

$$H_2O(t) = A_{H_2O}(t)e^{j(\omega_{H_2O}t + \varphi_{H_2O})} \quad (3)$$

If we now add another singlet to the water signal, then the modulus of the resulting signal, namely  $s(t)$ , is given by:

$$\|s(t)\| = \sqrt{(H_2O(t) + A(t))^*(H_2O(t) + A(t))} \quad (4)$$

where \* denotes the complex conjugate. For the sake of clarity, we will now name this new singlet  $A(t)$  “the metabolite”. Using Eqs. (1) and (3), the squared of Eq. (4) can be written:

$$\begin{aligned} \|s(t)\|^2 &= \left( A_{H_2O}(t)e^{-j(\omega_{H_2O}t + \varphi_{H_2O})} + A_0(t)e^{-j(\omega t + \varphi)} \right) \left( A_{H_2O}(t)e^{+j(\omega_{H_2O}t + \varphi_{H_2O})} + A_0(t)e^{+j(\omega t + \varphi)} \right) \\ &= A_{H_2O}^2(t) + A_0^2(t) + A_{H_2O}(t)A_0(t) \left( e^{-j(\omega_{H_2O}t + \varphi_{H_2O})} e^{+j(\omega t + \varphi)} + e^{+j(\omega_{H_2O}t + \varphi_{H_2O})} e^{-j(\omega t + \varphi)} \right) \\ &= A_{H_2O}^2(t) + A_0^2(t) + A_{H_2O}(t)A_0(t) \left( e^{+j((\omega - \omega_{H_2O})t + (\varphi - \varphi_{H_2O}))} + e^{-j((\omega - \omega_{H_2O})t + (\varphi - \varphi_{H_2O}))} \right) \\ &= A_{H_2O}^2(t) + A_0^2(t) + 2A_{H_2O}(t)A_0(t) \cos((\omega - \omega_{H_2O})t + (\varphi - \varphi_{H_2O})) \end{aligned} \quad (5)$$

Let's introduce  $\Delta\omega = (\omega - \omega_{\text{H}_2\text{O}})$  and  $\Delta\varphi = (\varphi - \varphi_{\text{H}_2\text{O}})$  corresponding respectively to the frequency and phase differences between the singlet and the water FID signals:

The first term,  $\text{FFT}(A_{\text{H}_2\text{O}}(t))$ , represents the original shape of the water peak centered on the zero frequency.

$$\begin{aligned} \|s(t)\|^2 &= A_{\text{H}_2\text{O}}^2(t) + A_0^2(t) + 2A_{\text{H}_2\text{O}}(t)A_0(t)\cos(\Delta\omega t + \Delta\varphi) \\ &= (A_{\text{H}_2\text{O}}(t) + A_0(t)\cos(\Delta\omega t + \Delta\varphi))^2 + A_0^2(t) - (A_0(t)\cos(\Delta\omega t + \Delta\varphi))^2 \\ &= (A_{\text{H}_2\text{O}}(t) + A_0(t)\cos(\Delta\omega t + \Delta\varphi))^2 + A_0^2(t)(1 - \cos^2(\Delta\omega t + \Delta\varphi)) \\ &= (A_{\text{H}_2\text{O}}(t) + A_0(t)\cos(\Delta\omega t + \Delta\varphi))^2 + (A_0(t)\sin(\Delta\omega t + \Delta\varphi))^2 \end{aligned} \quad (6)$$

$$\begin{aligned} \|s(t)\| &= \sqrt{(A_{\text{H}_2\text{O}}(t) + A_0(t)\cos(\Delta\omega t + \Delta\varphi))^2 + (A_0(t)\sin(\Delta\omega t + \Delta\varphi))^2} \\ &= (A_{\text{H}_2\text{O}}(t) + A_0(t)\cos(\Delta\omega t + \Delta\varphi))\sqrt{1 + \left(\frac{A_0(t)\sin(\Delta\omega t + \Delta\varphi)}{A_{\text{H}_2\text{O}}(t) + A_0(t)\cos(\Delta\omega t + \Delta\varphi)}\right)^2} \\ &= (A_{\text{H}_2\text{O}}(t) + A_0(t)\cos(\Delta\omega t + \Delta\varphi))\sqrt{1 + \varepsilon(t)} \end{aligned} \quad (7)$$

Assuming that

$$A_{\text{H}_2\text{O}}(t) \gg A_0(t) \quad (8)$$

(this will be the case for example in “none-” or “moderately-” water suppressed spectroscopy acquisitions), the term  $\varepsilon(t)$  can be neglected and the modulus of the signal can be approximated by:

$$\|s(t)\| \approx A_{\text{H}_2\text{O}}(t) + A_0(t)\cos(\Delta\omega t + \Delta\varphi) \quad (9)$$

The spectrum, namely  $S(\omega)$ , can be now obtained from the fast Fourier transformation of Eq. (9):

$$\begin{aligned} S(\omega) &\approx \text{FFT}(A_{\text{H}_2\text{O}}(t)) + \text{FFT}(A_0(t)\cos(\Delta\omega t + \Delta\varphi)) \\ &\approx \text{FFT}(A_{\text{H}_2\text{O}}(t)) + \text{FFT}(A_0(t)) \otimes \text{FFT}(\cos(\Delta\omega t + \Delta\varphi)) \end{aligned} \quad (10)$$

where  $\otimes$  denotes the convolution operation. The last term of the convolution can be expressed as:

$$\text{FFT}(\cos(\Delta\omega t + \Delta\varphi)) = \frac{(\delta(v - \Delta\omega) + \delta(v + \Delta\omega))e^{i\Delta\varphi}}{2} \quad (11)$$

where  $\delta$  denotes the Dirac function and Eq. (10) can then be written as:

$$\begin{aligned} S(\omega) &\approx \text{FFT}(A_{\text{H}_2\text{O}}(t)) + \text{FFT}\left(\frac{A_0(t)}{2}\right)e^{i\Delta\varphi} \\ &\quad \otimes (\delta(v - \Delta\omega) + \delta(v + \Delta\omega)) \end{aligned} \quad (12)$$

Let's analyze the different components of Eq. (12):

The first part of the convolution,  $\text{FFT}\left(\frac{A_0(t)}{2}\right)e^{i\Delta\varphi}$ , corresponds to half the metabolite resonance with a phase shift of  $\Delta\varphi = (\varphi - \varphi_{\text{H}_2\text{O}})$ , which is the original phase of the metabolite signal corrected by the original phase of the water signal (i.e. the original phase of the water signal is subtracted to the phase of the metabolite signal).

The last part of the convolution (including two  $\delta$  functions) implies that the metabolite resonance is split into two resonances located symmetrically around the water position, with a frequency shift of  $\Delta\omega = (\omega - \omega_{\text{H}_2\text{O}})$ . The original frequency of the metabolite is then shifted by the original water frequency.

In conclusion, the metabolite resonance is phased by using the water signal phase as reference and its frequency is shifted respectively to the water resonance frequency. It has to be noted that no assumption was made relatively to the shape of the signal  $A_0(t)$ . Therefore, as long as the assumption previously made in Eq. (8) remains valid [i.e. the term  $\varepsilon(t)$  can be neglected in Eq. (7)], considering the modulus of the FID signal does not change the shape of the peak composing this signal. The only effect is that the peak intensity is divided by a factor 2.

Noise considerations

*The noise of the FID signal*

Up to now, the calculation has been conducted ignoring the noise contribution. If we suppose that a noise, namely  $n(t)$ ,

**Table 1** Noise characteristics of the modulus ( $\|n(t)\|$ ) of the noise signal ( $n(t)$ ) in both Rayleigh and Gaussian conditions

	Noise mean value	Noise standard deviation
$n(t)$	0	$\sigma$
$\ n(t)\ $ Rayleigh case (SNR $\approx 0$ )	$\sigma\sqrt{\frac{\pi}{2}}$	$\sqrt{\frac{4-\pi}{2}}\sigma \approx 0.65\sigma$
$\ n(t)\ $ Gaussian case (SNR $> 3$ )	0	$\sigma$

is characterized by a zero mean Gaussian distribution with a standard deviation  $\sigma$  then, the modulus of the noise, namely  $\|n(t)\|$ , is Rice distributed [20]. Gudbjartsson and Patz [21] showed that for a signal to noise  $>3$ , the distribution of  $\|n(t)\|$  can be approximated by a Gaussian distribution whereas it follows a Rayleigh distribution when the signal tends towards zero. Table 1 shows the mean value and standard deviation of the modulus of the noise in both conditions.

Applying these approximations to an acquired FID signal leads to the following behavior: at the beginning of the FID, where the water signal is high, the modulus of the noise follows a Gaussian distribution, whereas at the end of the FID, when the water signal has disappeared, it follows a Rayleigh distribution. Figure 1 illustrates this property. Figure 1a shows the real part of a simulated noisy FID superimposed to its modulus. Simulation parameters are as follows: FID of 2 K time points, simulated by an

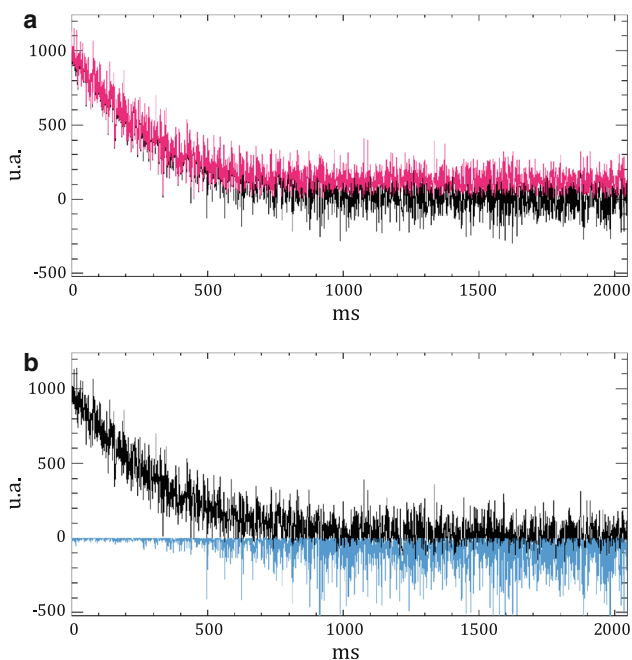


**Fig. 1** **a** Conventional noisy FID (black) and modulus of this FID (pink). When SNR is  $>3$  (beginning of the FID), the noise distribution of the modulus tends towards a Gaussian distribution whereas when SNR is nul (end of the FID), the noise distribution tends towards a Rayleigh distribution. **b** In blue, subtraction of the 2 FIDs

exponential decay function, with a first point value of 1,000, a spectral width (SW) of 1,000 Hz, a time decay of 3.14 ms. This time decay results, after fast Fourier transformation, into a resonance peak with a full width at half maximum (FWHM) of 1 Hz. Noise signal is simulated by  $2 \times 2$  K normally distributed pseudo random numbers with a mean of zero and a standard deviation of 100. We can observe that, at the beginning of the FID, both noise signals are very similar whereas at the end of the FID this is not the case anymore. Figure 1b, which shows the subtraction of these two signals (i.e. the conventional spectrum minus the modulus spectrum), illustrates more clearly this difference of behavior.

*The signal to noise of the resulting spectrum*

Let’s consider now the SNR of the spectrum obtained by fast Fourier transformation of a noisy FID  $s_n(t)$ . If we focus now on the Gaussian noise distribution, since modulus processing does not change the noise characteristics, the fast Fourier transformation of  $\|s_n(t)\|$  is equivalent to the fast Fourier transformation of the real part of the FID signal. Indeed, as previously shown from Eq. (12), the modulus signal is divided by a factor 2 when compared to the conventional signal. The resulting SNR is then expected to be divided by a factor  $\sqrt{2}$ .

The fast Fourier transformation of the Rayleigh section is much more difficult to calculate and only some assumptions will be presented here. In that case, the modulus of the noise  $\|n(t)\|$  can be considered as a noise signal with a standard deviation  $\sqrt{\frac{4-\pi}{2}}\sigma$  centered around a mean value of  $\sigma\sqrt{\frac{\pi}{2}}$  (see Table 1).

Hence  $\|n(t)\|$  can be expressed as follows:

$$\|n(t)\| = \sigma\sqrt{\frac{\pi}{2}} + \xi(t) \tag{13}$$

where  $\xi(t)$  denote a Rayleigh distributed noise, centered on zero.

Then, after fast Fourier transformation of the signal  $\|n(t)\|$ , we obtain:

$$\text{FFT}(\|n(t)\|) = \text{FFT}\left(\sigma\sqrt{\frac{\pi}{2}}\right) + \sum_{n=0}^N \xi(t)e^{-in\omega t} \tag{14}$$

where  $N$  denotes the number of time points.

The term  $\text{FFT}\left(\sigma\sqrt{\frac{\pi}{2}}\right)$ , the fast Fourier transformation of a constant, gives rise to an on-resonance Dirac peak which will be added to the water resonance peak, hence removed by the residual water suppression during the post-processing step.

**Table 2** Noise characteristics of the fast Fourier transformation of the modulus of a noisy signal ( $\|s_n(t)\|$ ) compared to the fast Fourier transformation of the conventional noisy signal ( $s_n(t)$ ) in both Rayleigh and Gaussian conditions

	Signal intensity	Noise mean value	Noise standard deviation	Signal to noise
FFT( $s_n(t)$ )	$I$	0	$\sigma\sqrt{N}$	$\frac{I}{\sigma\sqrt{N}}$
FFT( $\ s_n(t)\ $ ) (Rayleigh)	$\frac{I}{2}$	0	$\sigma\sqrt{\frac{N(4-\pi)}{4}} \approx 0.46\sigma\sqrt{N}$	$\frac{I}{\sigma\sqrt{N(4-\pi)}} \approx 1.08 \frac{I}{\sigma\sqrt{N}}$
FFT( $\ s_n(t)\ $ ) (Gaussian)	$\frac{I}{2}$	0	$\sigma\sqrt{\frac{N}{2}} \approx 0.7\sigma\sqrt{N}$	$\frac{I}{\sigma\sqrt{2N}} \approx 0.7 \frac{I}{\sigma\sqrt{N}}$

Concerning the second term of Eq. (14), the phase rotation involved by the fast Fourier transformation will spread the phase of each point of the noise signal before adding them all together. Therefore, this second term can be assimilated to a new noise distribution with a mean value equal to zero. Concerning the standard deviation of this new noise distribution, since the number of points involved in this calculation is significant (typically  $N = 1,024$  points), the central limit theorem can be applied here. The noise standard deviation of this new noise, namely  $\tilde{\sigma}$ , can then be approximated by:

$$\tilde{\sigma} = \sqrt{\sum_{n=0}^N \sigma_n^2} = \sigma\sqrt{\frac{N(4-\pi)}{4}} \tag{15}$$

Table 2 reports the mean value and the standard deviation of the fast Fourier transformation of the noisy FID  $s_n(t)$  obtained with conventional and with modulus processing in both Rayleigh and Gaussian conditions.

Applying the approximations recapitulated in Table 2 to an acquired FID signal leads to the following situation: at the beginning of the FID, when SNR is high, modulus processing will decrease the SNR of the resulting spectrum by a factor  $\sqrt{2}$  when compared to conventional processing. This corresponds to a decrease in SNR of 30 %. At the end of the FID, when there is no signal at all, the modulus will only have a slight effect on the SNR of the spectrum.

The SNR of the resulting spectrum is hence depending on whether the Gaussian or Rayleigh condition is

predominant on the FID. This means that both acquisition time and time domain filtering parameters will drastically affect the SNR resulting from modulus processing, when compared to conventional processing. With a long acquisition time and without time filtering, the Rayleigh component will dominate and the SNR of the resulting spectrum will only be marginally affected. However, if a short acquisition time is chosen, or if a hard time filter is applied, then the Gaussian section will be dominant and a drop of  $\sqrt{2}$  is expected in the SNR of the resulting spectrum. The simulations shown in the next section will confirm these hypotheses.

As a general conclusion in regards to the noise consideration, the SNR of the resulting spectrum obtained using modulus versus conventional processing is expected to be between “equivalent” and “divided by  $\sqrt{2}$ ”, depending on the parameters selected for the acquisition time and for the time filtering.

#### Contamination estimation

In Eq. (8), we have made the following approximation: the water signal is drastically higher than the other signals present in the FID. Let’s now estimate what will be the consequences if this condition is not fulfilled. This may for example occur in the presence of strong lipids signals arising from the skull in brain MR spectroscopy. Using the Taylor expansion of the square root, Eq. (7) can be written as follows:

$$\begin{aligned} \|s(t)\| &= (A_{H_2O}(t) + A_0(t) \cos(\Omega(t))) \left( 1 + \frac{1}{2} \varepsilon(t) - \frac{1}{8} \varepsilon^2(t) + \dots \right) \\ &= (A_{H_2O}(t) + A_0(t) \cos(\Omega(t))) \left( 1 + \frac{1}{2} \left( \frac{A_0(t) \sin(\Omega(t))}{A_{H_2O}(t) + A_0(t) \cos(\Omega(t))} \right)^2 - \frac{1}{8} (\dots)^4 + \dots \right) \\ &= A_{H_2O}(t) + A_0(t) \cos(\Omega(t)) + \frac{(A_0(t) \sin(\Omega(t)))^2}{2(A_{H_2O}(t) + A_0(t) \cos(\Omega(t)))} - \frac{1}{8} \dots \end{aligned} \tag{16}$$



where the term  $\Omega(t) = \Delta\omega t + \Delta\varphi$ , including both frequency and phase shifts, is introduced in order to improve the readability. As a first approximation, we can take into account only the first term of the Taylor series:

$$\begin{aligned} \varepsilon(t) &\approx \frac{(A_0(t) \sin(\Omega(t)))^2}{2(A_{H_2O}(t) + A_0(t) \cos(\Omega(t)))} \\ &= \frac{(A_0(t) \sin(\Omega(t)))^2}{2A_{H_2O}(t)} \times \frac{1}{1 + \frac{A_0(t)}{A_{H_2O}(t)} \cos(\Omega(t))} \end{aligned} \quad (17)$$

As a second approximation, we can again simplify this equation assuming that  $\frac{A_0(t)}{A_{H_2O}(t)} \ll 1$ . The error  $\varepsilon(t)$  can then be approximated by:

$$\begin{aligned} \varepsilon(t) &\approx \frac{(A_0(t) \sin(\Omega(t)))^2}{2A_{H_2O}(t)} = \frac{A_0^2(t)(1 - \cos(2\Omega(t)))}{4A_{H_2O}(t)} \\ &= \frac{A_0^2(t)}{4A_{H_2O}(t)} - \frac{A_0^2(t) \cos(2\Omega(t))}{4A_{H_2O}(t)} \end{aligned} \quad (18)$$

If we look at the fast Fourier transformation  $E(\omega)$  of  $\varepsilon(t)$ , then using the mathematical development already used for Eqs. (10), (11) and (12), the maximum error in the frequency domain can be estimated by:

$$\begin{aligned} E(\omega) &\approx \text{FFT}\left(\frac{A_0^2(t)}{4A_{H_2O}(t)}\right) - \text{FFT}\left(\frac{A_0^2(t)}{4A_{H_2O}(t)}\right) \\ &\quad \otimes \frac{1}{2}(\delta(v - 2\omega) + \delta(v + 2\omega))e^{i\Delta\varphi} \end{aligned} \quad (19)$$

The first term of Eq. (19) leads to an on-resonance contamination peak at the water resonance. The second term leads to a contamination shifted relatively to the water resonance by two times the relative frequency shift between the metabolite and the water resonances. The second term indicates that the contamination peak will be superimposed to the spectrum at twice the original frequency of the signal  $A(t)$ . The sign “minus” preceding this second term means that this contamination peak has an opposite sign when compared to the original peak (i.e. is inverted relatively to the original peak). The same mathematical development can be applied to all the terms of the Taylor series [Eq. (16)]. The resulting contaminations pattern consists on a succession of alternate positive/negative resonances harmonics at frequency  $2\omega, 3\omega, 4\omega, \dots$  decreasing in intensity.

Since the first point of the FID corresponds to the area of the peak obtained after fast Fourier transformation, we can estimate that the area of the contamination of the first harmonic peak is inferior to  $\frac{A_0^2(0)}{8A_{H_2O}(0)}$ . Therefore, if the area of the water peak is 10 times higher than the metabolites one, the area of the contamination peak will be <1.25 % the area of metabolites. Figure 2 shows the upper limit of the expected area of this contamination peak

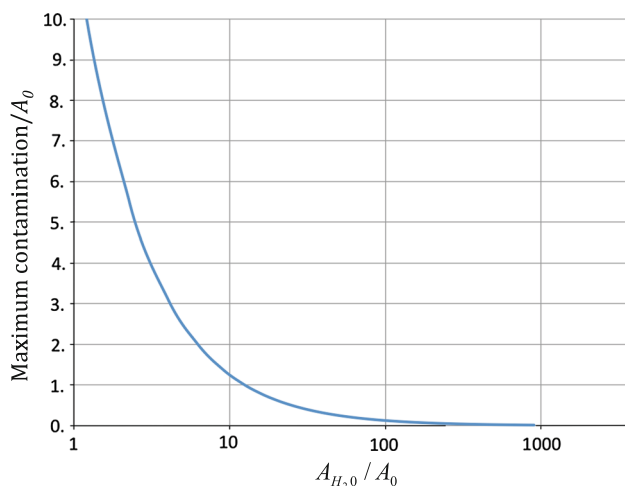


**Fig. 2** Illustration of the variation of the maximum contamination level as a function of  $A_{H_2O}/A_0$  ratio. In this graph, the contamination is expressed as the maximum area of this contamination (i.e. first harmonic peak) divided by the area of the metabolite (i.e.  $A_0$ )

respectively to  $A_{H_2O}/A_0$  area. If no water suppression is performed before the acquisition, since the water concentration is supposed to be approximately  $10^5$  higher than the metabolites concentration, the area of the contamination peak is expected to be  $<1.25 \cdot 10^{-4}$  % the metabolites area, which is significantly inferior to the noise contribution.

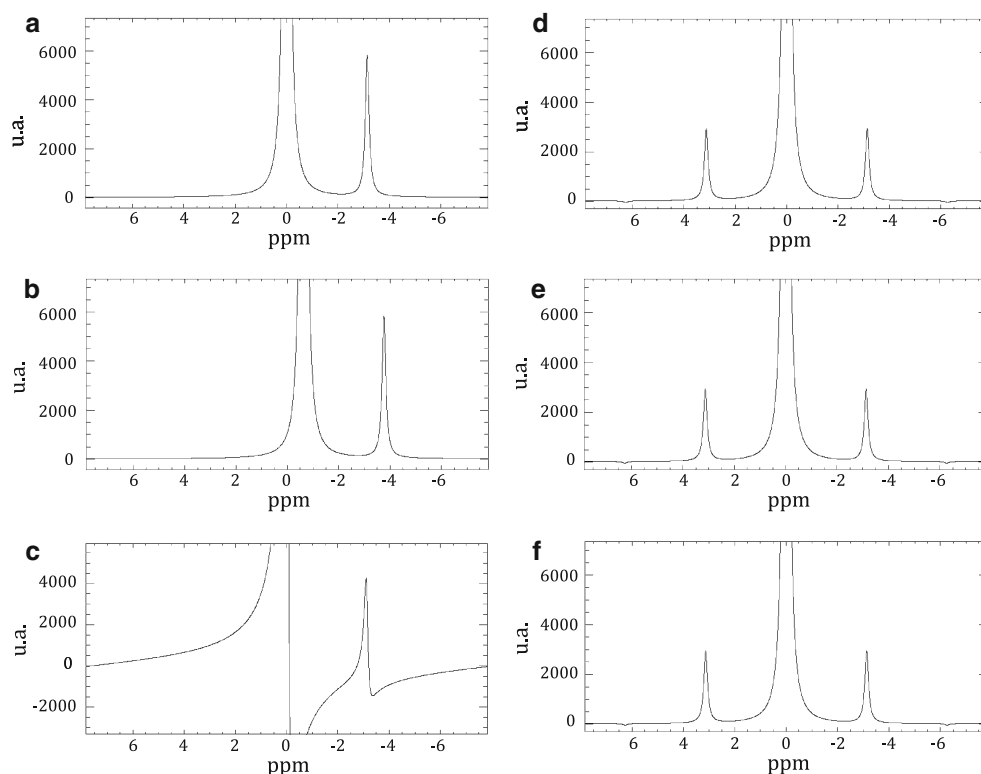
Simulations have been performed in order to validate these hypotheses, as shown in the following section.

### Experimental setting for in vivo applications

In vivo experiments have also been performed on a 3T MR scanner (Verio, Siemens Medical Solution, Erlanger, Germany). Most of the spectra presented in the results section are extracted from a  $25 \times 25$  circular weighted short echo time CSI experiment with moderate water suppression. Acquisition parameters are: TR/TE = 1,500/16 ms, 2 K time points, SW = 2,000 Hz. The field of view is  $240 \times 240$  mm and the slice is 20 mm thick. Total acquisition time is 11 min 7 s. Some long echo time CSI experiments are also presented (with an echo time of 135 ms, all other parameters remain identical). Post-processing consists in applying a Hanning spatial filtering, zero filling the acquired data to 8 K points in the time domain and removing the residual water signal using the HLSVD technique [22].

In order to validate experimentally the gain in SNR obtained using the modulus processing in the case of subject motion, a mono-voxel PRESS spectroscopic experiment is also presented. In this case acquisition parameters are: TR/TE = 1,500/30 ms, 1 K time points, SW = 2,000 Hz, a voxel size of  $20 \times 20 \times 20$  mm<sup>3</sup>, 128

**Fig. 3** Illustration of the phase and frequency shift modification induced by the modulus processing. *Spectra on the left* show the result obtained after conventional processing. *Spectra on the right* show the result obtained after modulus processing. **a, d** Simulation of a water peak phased and on-resonance. **b, e** Simulation of a water peak phased and off-resonance. **c, f** Simulation of a water peak dephased and on-resonance. In these three cases, the correction for phase and frequency shifts is successfully performed by the modulus processing (see **d–f**)



accumulations, resulting in a total acquisition time of 3 min 12 s. Post-processing includes fast Fourier transformation and residual water removal.

## Results

### Simulations

#### *The FID signal*

In order to illustrate the phase and frequency shift correction, we have simulated several situations. FIDs were simulated using IDL software (Interactive Data Language, Research Systems Inc., Boulder, CO, USA). They were further processed with CSIAPO, a tool that we have previously developed [18]. Two FIDs of 4 K complex points with a time decay of 31.4 ms, a SW of 1,000 Hz and a zero-phase were generated. The first FID, with a starting value of 2,000, is on-resonance and is supposed to simulate the water signal. This FID, with a time decay of 31.4 ms results, after fast Fourier transformation, in a resonance signal with a FWHM of 10 Hz, which is comparable to the value typically obtained for the water signal in vivo. The second FID, with a starting value of 200 and a frequency shift of 200 Hz, acts as a metabolite signal. The simulated water intensity is hence 10 times higher than the simulated

metabolite resonance. The simulated ratio between the water and metabolite signals is inferior to the situation observed in vivo and can hence be assimilated to an acquisition with a moderate water suppression. Figure 3 illustrates the phase and frequency shift correction relatively to the water signal. As expected, phase and frequency shift are adequately corrected by modulus processing. In Fig. 3a, water and metabolite signals are phased and on-resonance. In Fig. 3b, water and metabolite signals are phased but shifted by a frequency of 40 Hz. In Fig. 3c, water and metabolite signals are shifted in phase by  $40^\circ$  and on-resonance. The right column of this figure shows that, using modulus processing, phase and frequency shift are successfully corrected and the 3 resulting spectra are identical (Fig. 3d–f).

Figure 4a shows a modulus spectrum multiplied by a factor of 2 and superimposed to the conventional one. This spectrum simulates a water peak and several metabolites with different amplitudes, phases and chemical shifts. Figure 4b shows the result obtained after subtracting the conventional spectrum from 2 times the modulus one. If we focus on the spectral part at the right of the water signal (i.e. between 0 and  $-7$  ppm) including the peaks of interest, we cannot observe any residue on the subtracted spectrum. This result confirms that modulus processing, in agreement with the theory, does not modify the linewidth and line shape of the peaks.



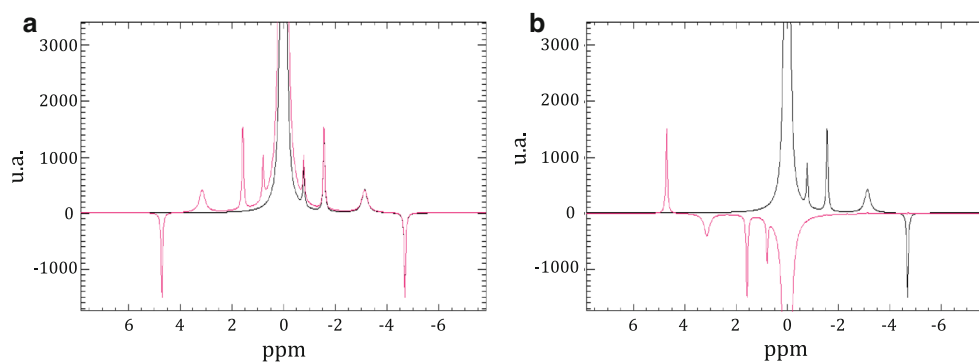


**Fig. 4 a** Comparison of a simulated spectrum obtained with conventional processing (*black*) and twice the spectrum obtained after modulus processing of the same simulated signal (*pink*). **b** Subtraction of these 2 spectra. The subtraction does not show any

residue on the spectral range including the signals of interest simulating the metabolites (i.e. between 0 and  $-8$  ppm). This confirms that the linewidth and the lineshape are not modified by the modulus processing

### The noise on the FID

In order to validate the noise modification induced by modulus processing, a first simulation was performed. A complex noise signal composed of  $2 \times 4$  K normally distributed pseudo random numbers with a mean of zero and a standard deviation of 10 was generated. The Rayleigh condition was first checked using this noise signal. In order to fulfill the Gaussian condition, a second signal was generated by adding to this noise a constant signal with an amplitude of 1,000. After fast Fourier transformation, this constant signal gives a Dirac peak at the zero frequency, which we excluded from the spectral region used for the calculation of the noise mean value and standard deviation. These simulations were repeated 1,000 times. Table 3 reports the mean value and standard deviation of the noise calculated from these 1,000 simulations. The results obtained from these simulations are very close to the theoretical values (see Table 1).

**Table 3** Noise characteristics before and after fast Fourier transformation calculated from a noise signal simulating the Rayleigh and Gaussian conditions

	Noise mean $\pm$ SD	FFT (noise) mean $\pm$ SD
Conventional	0.00 $\pm$ 10.00 (0.00 $\pm$ 10.00)	0.02 $\pm$ 640.1 (0.00 $\pm$ 640)
$\ n(t)\ $ Rayleigh	12.54 $\pm$ 6.55 (12.53 $\pm$ 6.55)	0.01 $\pm$ 296.3 (0.00 $\pm$ 296.5)
$\ n(t)\ $ Gaussian	0.00 $\pm$ 10.00 (0.00 $\pm$ 10.00)	0.34 $\pm$ 452.4 (0.00 $\pm$ 452.6)

The values of [mean  $\pm$  standard deviation (SD)] reported in this table were calculated from 1,000 simulations. The values indicated between parentheses denote the theoretical values

### The signal to noise of the resulting spectrum

In order to check the SNR assumption exposed in the “Materials and methods” section, (“The signal to noise of the resulting spectrum”), a second simulation has been performed. For this purpose, a signal composed of a water FID, a metabolite FID and a noise signal was generated. First, two FIDs with the characteristics previously described (see section “The FID signal”) were added. Second, a complex noise signal with the characteristics previously described (i.e. 4 K points, a mean value of 0, a standard deviation of 10) was added to these FIDs, giving rise to the desired simulated signal, now called composite signal.

As previously, the Rayleigh condition was first simulated using this resulting composite signal. Second, in order to simulate the Gaussian condition, a constant signal of amplitude 1,000 was added to the composite signal. It is clear that in the first case, the Rayleigh condition is not totally fulfilled because the first portion of the noise signal is superimposed to the FID signal. However, most of the composite signal fulfills the Rayleigh condition and we can at least assume that the standard deviation measured on this simulation is under-estimated due to the Gaussian condition characterizing the first part of the noise signal. Table 4 compares with the theoretical values (Table 2) the results obtained when this simulation is repeated 1,000 times.

We can now calculate the SNR obtained in the case of modulus processing versus conventional processing for different values of temporal filtering and acquisition time. In order to achieve this, the simulated composite signal was first filtered with an exponential decaying function with several line broadening values (LB). Table 5 shows the results obtained for LB values of 2, 1 and 0.5 Hz, corresponding respectively to a time decay of 159, 317 and 635 ms. Table 6 shows the results obtained at different

**Table 4** Noise standard deviation and SNR calculated from the composite signal simulating Rayleigh and Gaussian conditions

	Signal (amplitude)	Noise (SD)	SNR
<b>Conventional</b>			
Measured	7,463.0	640.2	11.66
(calculated)		(640.0)	(11.66)
<b>Modulus Rayleigh</b>			
Measured	3,746.2	303.9	12.32
(calculated)	(3,731.5)	(296.5)	(12.59)
<b>Modulus Gaussian</b>			
Measured	4,045.7	452.4	8.94
(calculated)	(3,731.5)	(452.5)	(8.24)

The values reported here were calculated from 1,000 simulations. The values indicated in parentheses denote the theoretical values

**Table 5** Comparison of SNR obtained with modulus versus conventional processing for different filter LB values

LB (Hz)	2	1	0.5	None
SNR (conventional)	61.81	47.57	35.61	11.66
SNR (modulus)	47.22	38.94	31.82	12.34
Conventional/modulus	1.31	1.22	1.12	0.94

**Table 6** Comparison of SNR obtained with modulus versus conventional processing for different acquisition times, without temporal filtering

Acquisition time (ms)	127	255	511	1,023	4,095
SNR (conventional)	52.65	37.36	28.75	20.84	11.66
SNR (modulus)	38.24	30.58	26.65	20.89	12.34
Conventional/modulus	1.38	1.22	1.08	1.00	0.94

acquisition times (in the range 127–4,096 ms), without temporal filtering.

These results confirm that the better the Rayleigh condition is fulfilled, the closer the SNR values resulting from conventional and modulus processing. Since the goal is to get the best possible SNR, these results also indicate that modulus processing is of interest only if the gain in SNR resulting from both phase and frequency shift corrections at least compensates for the loss introduced by modulus processing.

### Estimation of contaminations

Simulations have also been performed in order to check the assumption regarding the error introduced by the approximation made in Eq. (8). Figure 5 illustrates the contamination that can occur after conventional and modulus processing when the condition  $A_{\text{H}_2\text{O}} \gg A_0$  is not fulfilled. In order to simulate this situation, we have changed the

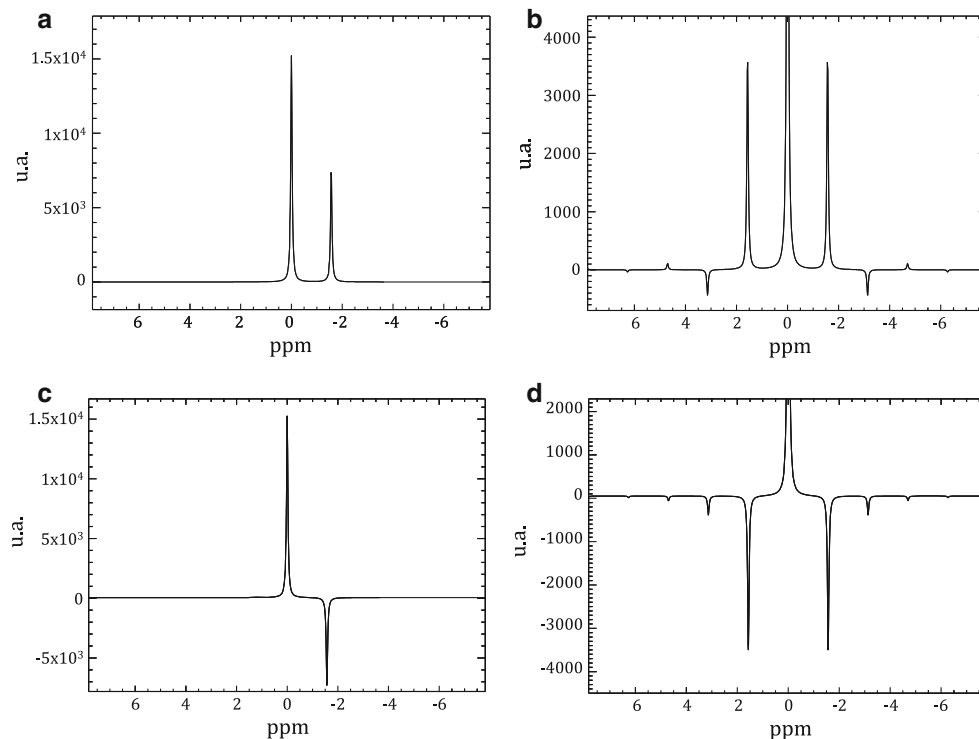
starting values of the two FIDs described in previous section “The FID signal”. The first point of the water FID was arbitrarily fixed at  $1 \times 10^5$  a.u. and the first point of the metabolite FID at  $5 \times 10^4$  a.u. The left column of Fig. 5 shows the spectrum obtained with conventional processing, the right column the pattern obtained with modulus processing. With these first point values, and according to Eq. (19), the expected contamination area of the first harmonic should be less than  $3.12 \times 10^3$  a.u. The area of the first harmonic contamination (at 3.17 ppm) measured on Fig. 5b is  $2.91 \times 10^3$  a.u. The other smaller contaminations (at 4.76 and 6.34 ppm) come from the terms that we have neglected in Eq. (16) (i.e. harmonics at higher frequencies). Figure 5d shows the contamination pattern obtained when the metabolite and the water signal have an opposite sign. Table 7 reports the measured contamination for different ratios between water and metabolite signal areas (where the area is indeed equal to the first point of the FIDs).

Figure 6 shows what would be the contamination in the case of a strong lipid resonance. As seen in this figure, the water peak would then be enlarged by the on-resonance contamination [first part of Eq. (19)] while, as the resonance frequencies of the lipids are downfield when compared to other metabolites, the other harmonics would arise outside the metabolites region of interest. This simulation confirms the deduction we have made from Eq. (19).

### In vivo results

In this section we show some applications of modulus processing to data acquired in vivo. Brain in vivo MR spectroscopic data were acquired on volunteers on a 3T Verio MR system (Siemens Medical Solutions, Erlangen, Germany) using a home-designed OVS-CSI pulse sequence described previously [18]. Acquisition and processing parameters are described in the “Materials and methods” section, (“Experimental settings for in vivo applications”).

Figure 7 shows an example of spectrum extracted from a short echo time CSI experiment. Before suppression, the area of the residual water signal was approximately 40 times higher than the area of the NAA resonance. Figure 7a shows the modulus (in pink color) and the conventional (in black color) spectra obtained from the same voxel. The modulus spectrum was multiplied by a factor 2 in order to compensate for the signal loss induced by modulus processing. As observed on the left part of the conventional spectrum (around 8 and 10 ppm resonances), the residual water signal is strong enough to create sidebands. According to the theory, the sidebands are located symmetrically to the water resonance. Therefore, in addition to the sidebands observed on the left part of the spectrum, we also expect antisymmetrical sidebands on the right part of the spectrum, hence falling in the region of interest. While



**Fig. 5** Illustration of the contamination that can occur when the term  $\varepsilon(t)$  in Eq. (7) is not negligible (i.e. the condition  $A_{\text{H}_2\text{O}} \gg A_0$  is not fulfilled). The figure illustrates the following contamination pattern

**Table 7** Comparison of the area of the first harmonic contamination for different ratios between water and metabolite peak areas

<b>Water signal area (a.u.)</b>	$1.0 \times 10^5$	$1.0 \times 10^5$	$1.0 \times 10^5$
<b>Metabolite signal area (a.u.)</b>	$5.0 \times 10^4$	$2.5 \times 10^4$	$1.0 \times 10^4$
<b>First contamination area (a.u.)</b>			
Measured	$2.91 \times 10^3$	$7.59 \times 10^2$	$1.18 \times 10^2$
(calculated)	$(3.12 \times 10^3)$	$(7.81 \times 10^2)$	$(1.25 \times 10^2)$
<b>Contamination/metabolite %</b>			
Measured	5.82	3.03	1.18
(calculated)	(6.24)	(3.12)	(1.25)

The last line of the table shows the resulting percentage of the contamination area when compared to the metabolite signal area

the couple of sidebands observed at 10 and 0 ppm only corrupt the baseline, the ones at 8.2 and 1.8 ppm are superimposed to the  $\text{CH}_2$  resonance of the lipid signal and hence compromise the quantitation of this peak. Figure 7b compares the conventional spectrum (in black color) and the result of the subtraction between the conventional spectrum and twice the modulus spectrum. The subtraction clearly shows the sidebands which were previously superimposed to the conventional spectrum. As

after conventional (*left column*) and modulus (*right column*) processing. **a, b** The metabolite and water phases are identical; **c, d** the metabolite and water phases are opposite

demonstrated by Serrai et al. [19], modulus processing solves this problem by removing these sidebands and then quantification becomes possible. Our in vivo results illustrate again convincingly the advantage of modulus versus conventional technique to overcome the problems due to the presence of sidebands. Furthermore one can see on Fig. 7 that the SNR is comparable between these two spectra. This is confirmed by calculations: the SNR is 200 for the NAA signal on the conventional spectrum versus 186 for the modulus spectrum, which corresponds to a loss of 7 % only. It has to be noted that a small residue can be observed on the subtracted spectrum under the NAA (2.02 ppm) and creatine (3.04 ppm) peaks. This is not in agreement with the results we have obtained on the simulation (Fig. 4) and this point will be discussed later on.

Figure 8 shows an example of spectra extracted from another short echo time CSI experiment acquired with a moderate and without water suppression. Figure 8a, b show the spectra obtained without water suppression using conventional (Fig. 8a) and modulus (Fig. 8b) processings. In both cases, the water resonance is removed during the post-processing using HLSVD technique [22]. The bottom of Fig. 8 compares a spectrum acquired without water suppression (Fig. 8d) using modulus processing to a spectrum from the same location but acquired with moderate water suppression (Fig. 8c) using conventional processing. As

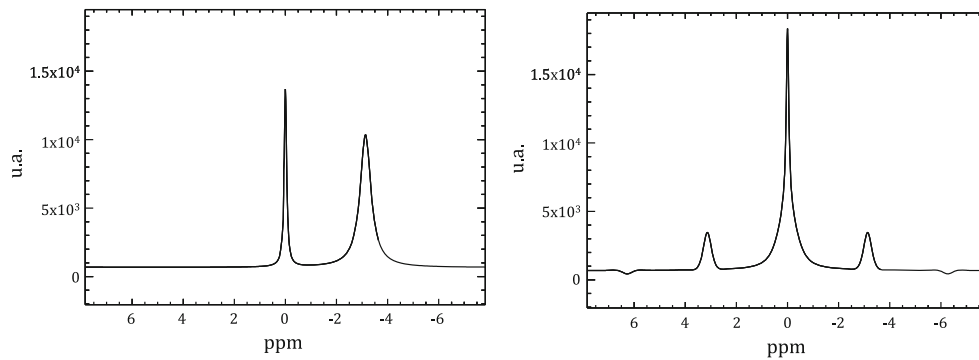


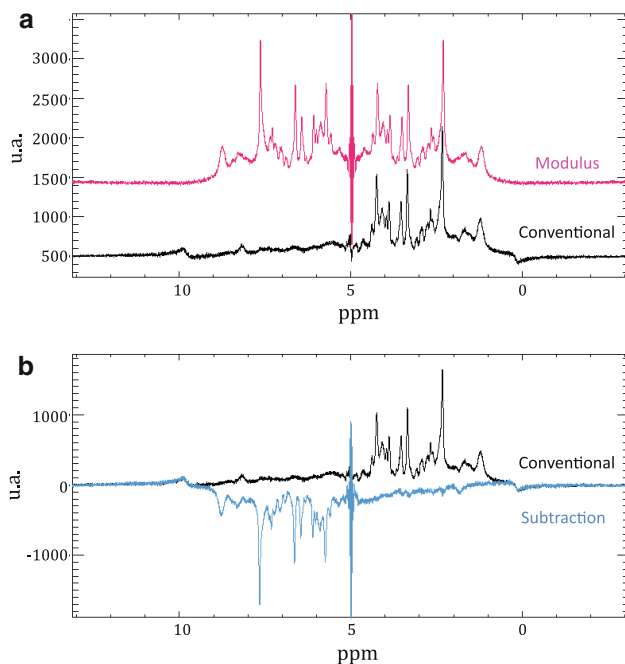
**Fig. 6** Illustration of the contamination due to a strong lipid signal resonance. In the case of modulus processing, the water peak is enlarged by the on-resonance contamination [first term of Eq. (19)]. If

the water signal needs to be quantified, this has to be done using conventional processing

previously reported by Serrai et al. [19], the severe baseline distortions due to sidebands (Fig. 8a) are successfully removed by modulus processing (Fig. 8b, d).

Figure 9 shows how modulus processing can reduce motion artifacts. A volunteer was asked to slowly move his head during the acquisition of 128 scans in a mono-voxel PRESS spectroscopic experiment with moderate water suppression. Figure 9a shows the spectrum obtained by simply adding all the original FIDs together whereas

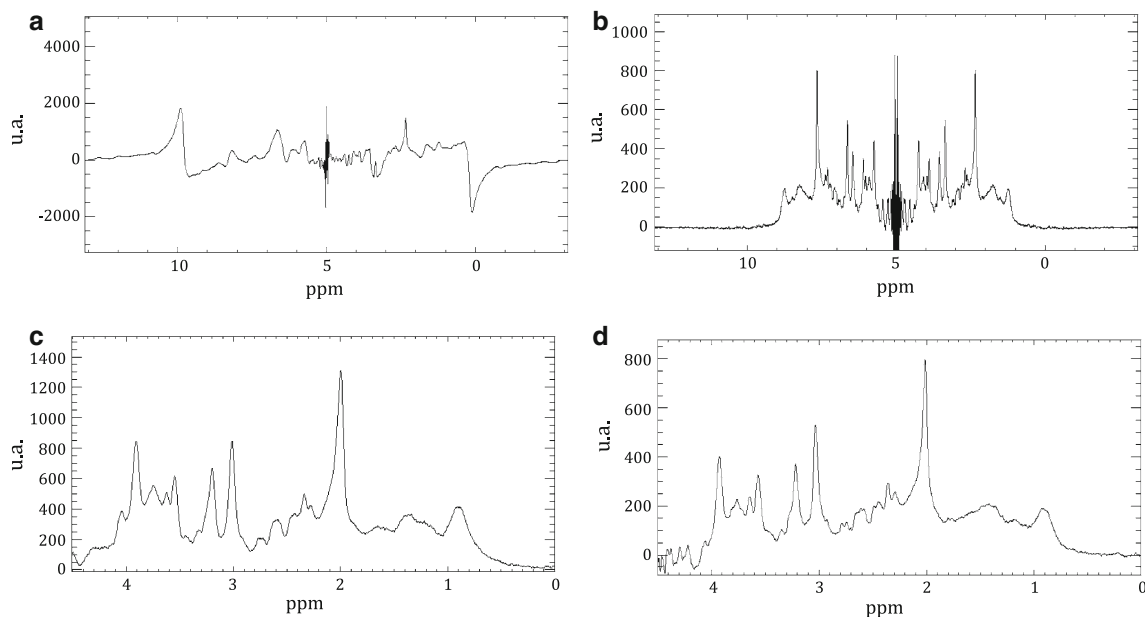
Fig. 9b shows the spectrum obtained by adding the modulus of the same collection of FIDs. The SNR of the NAA peak is 118 for the conventional spectrum and 199 for the modulus spectrum. After exponential time filtering with a LB value of 1 Hz, the SNR of the NAA peak is 313 for the conventional spectrum versus 360 for the modulus spectrum. The SNR is hence increased by 15 % in the case of modulus processing. Furthermore, the fact that each FID is frequency realigned before summation leads to a great improvement (narrowing) in linewidth. This can be clearly observed when comparing the NAA (2.02 ppm) or creatine/choline (3.02/3.2 ppm) peaks on the modulus spectrum to the conventional spectrum.



**Fig. 7** Comparison of brain spectra obtained using conventional versus modulus processing. **a** Example of spectra obtained using the conventional (black) and the modulus (pink) processing. The modulus spectrum is multiplied by a factor 2. In the conventional case, the sidebands can be easily identified on the left part of the spectrum. **b** Subtraction of twice the modulus spectrum from the conventional spectrum. The resulting spectrum (blue) reveals the sidebands which were previously hidden under the spectrum

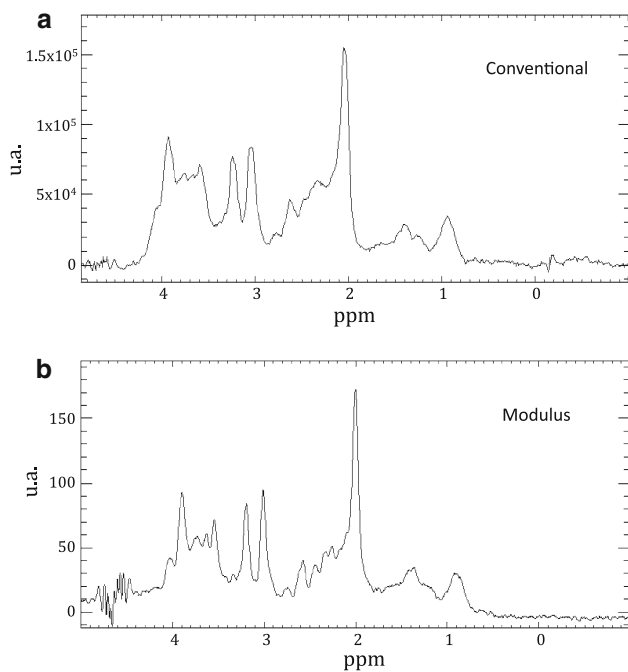
Figure 10 illustrates how modulus processing can be applied to the combination of signals acquired with phased array coils. The two spectra shown on this figure are extracted from a long echo time CSI experiment. Figure 10a shows the spectrum obtained with the coil combination provided by the manufacturer (using the phase of the first point of the FID). Figure 10b shows the spectrum obtained using the phase and frequency shift correction provided by our modulus processing. Coil amplification correction was performed using  $B_1$  maps calculated by fitting the residual water signal using the AMARES technique for each voxel and for each coil, using conventional processing. The SNR for the NAA peak is 78 with conventional processing versus 100 with modulus processing, which corresponds to an increase of 28 %. After filtering the FID signal with an exponential function with  $LB = 1$  Hz, the SNR of the NAA peak is 176 in the conventional spectrum and 169 in the modulus spectrum, hence resulting in a decrease of only 4 %.

Figure 11 illustrates the automatic  $B_0$  spatial shift correction performed by modulus processing. Figure 11a, b show spectra from two voxels extracted from a short echo time CSI experiment. The circles superimposed on the MR image show the position, size and shape of both selected voxels. Figure 11a shows the spectra obtained from these two voxels



**Fig. 8** Comparison of the conventional (**a**) and the modulus spectra (**b, d**) obtained without water suppression with the conventional spectrum obtained with a moderate water suppression (**c**). **a** The conventional spectrum obtained without water suppression during acquisition (water signal is removed during post-processing). In that

case, the sidebands and baseline distortions are so important that the spectrum cannot be quantified. **b** The modulus spectrum acquired in the same conditions. **c, d** Show respectively the conventional spectrum obtained with a moderate water suppression and the modulus spectrum obtained without water suppression



**Fig. 9** **a** Spectrum obtained by adding the 128 original FIDs collected during patient motion and **b** spectrum obtained by adding the modulus of the same collection of FIDs. The decrease in the line width observed in the modulus spectrum illustrates the frequency shift correction provided by modulus processing

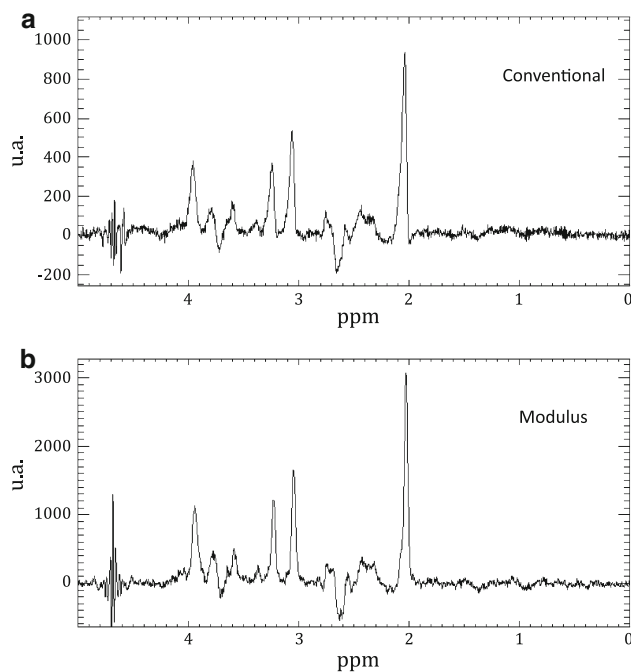


**Fig. 10** Illustration of the application of modulus processing to a recombination of signals collected from phased array coils. **a** Spectrum from a CSI experiment using the first point to correct for the phase shift between the coils. **b** Shows the spectrum from the same voxel using modulus processing for phase correction

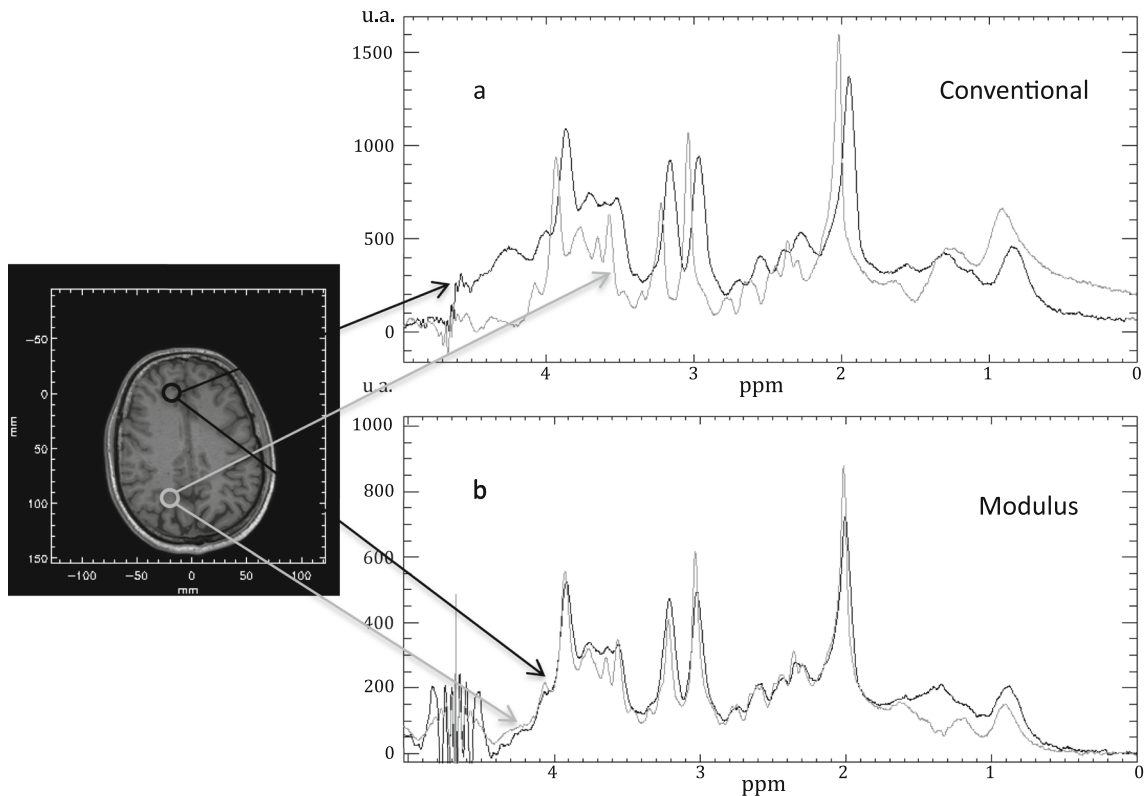


**Fig. 11** Illustration of the  $B_0$  shift correction performed by modulus processing. **a** Shows 2 conventional spectra from 2 different voxels of a CSI experiment. **b** Shows the modulus spectra obtained from these

two voxels. The *two circles* superimposed on the MR image show the position, size and shape of the two selected voxels

using conventional processing. Figure 11b shows the spectra from the same voxels obtained after modulus processing. As shown on this figure, the frequency shift due to  $B_0$  spatial variation is successfully removed by modulus processing.

Figure 12 shows how a spectrum contaminated by a large lipid resonance from the skull is affected by modulus processing. Figure 12a shows a spectrum extracted from a short echo time CSI experiment contaminated by a lipid resonance originating from the skull. The reference peak is not high enough when compared to the lipid resonance and hence the approximation made in Eq. (8) is not valid any more. Figure 12b shows that part of the lipid resonance is shifted to zero frequency and is superimposed to the water resonance. This is in total agreement with Eq. (19).

Figure 13 presents metabolite maps obtained applying modulus processing to a long echo time CSI. The coil combination is performed using the scheme described in references [23, 24]. The only difference here is that the phase of the signal from each coil is aligned using modulus processing. The way the metabolites maps are calculated is described in Ref. [18]. Figure 13a shows the conventional MR image used as reference for the CSI experiment (same field of view, same slice position). Figure 13b–d show respectively the NAA, creatine and choline metabolic maps superimposed to the MR image. Figure 13e–g show the three

metabolites maps obtained from the same experiment using conventional processing. These maps are slightly different from the maps obtained using modulus processing. This may be due to the lack of correction of sidebands, phase and frequency shift in the case of conventional processing. It has to be noted that NAA, creatine and choline maps obtained using modulus processing are in better agreement with the literature (see [25] for example). The grid bands superimposed on all the images represent the outer volume saturation bands used for eliminating the lipid signal from the skull. This example illustrates the fact that modulus processing does not introduce any artifact to the automatic fitting procedure, even near the skull where the resulting lipid signal intensity is high, as previously illustrated by Fig. 12.

## Discussion

Since the SNR is a key point in NMR spectroscopy, the loss of  $\sqrt{2}$  in SNR resulting theoretically from the application of the modulus technique could be considered as a disadvantage. However, this predicted loss was never observed when applying the modulus technique to in vivo data in our practice. One of the reasons possibly leading to this positive observation, that we have not introduced yet,



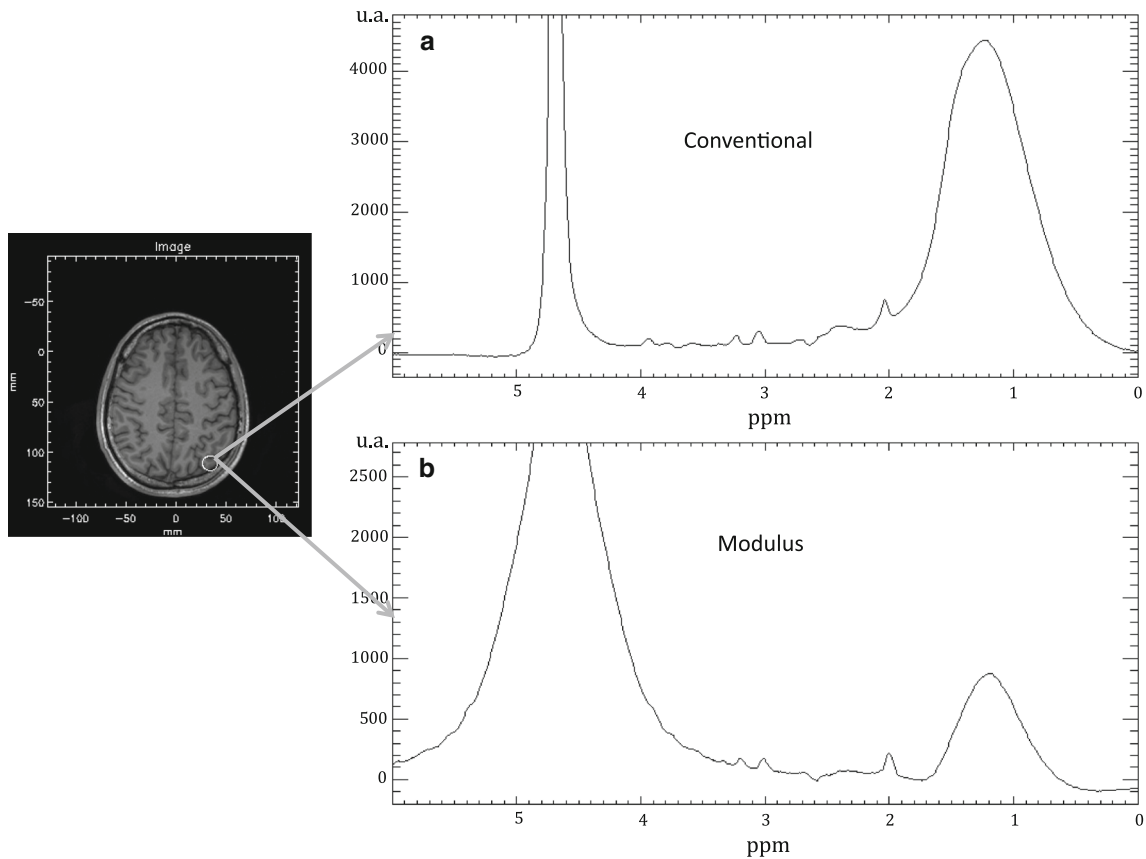


**Fig. 12** **a** Shows a spectrum contaminated by a lipid signal originating from the skull. On **b** we can see how the spectrum of the same signal is modified by modulus processing. The *circle* superimposed on the MR image shows the selected voxel

could be the ability of modulus processing to also correct for eddy currents. Indeed, the term  $(\omega_{\text{H}_2\text{O}}t + \varphi_{\text{H}_2\text{O}})$  in Eq. (3) can be replaced by  $\Phi(t)$ , where  $\Phi$  denotes a time-dependent phase shift. Since there is no constraint forcing  $\Phi(t)$  to be a linear function, this term  $\Phi(t)$  could include both the resonance frequency of the water and a phase shift induced by eddy currents. If we introduce the same notation for the metabolite signal, Eq. (9) can then be written:

$$\|s(t)\| = A_{\text{H}_2\text{O}}(t) + A_0(t) \cos(\Phi(t) - \Phi_{\text{H}_2\text{O}}(t))$$

This equation represents the real part of the equation proposed by Klose [26] for eddy current correction, which means that the peak shape distortions due to eddy currents or by any other source of phase distortion, will be also corrected. This could be one of the explanations for the difference in SNR observed between the simulations and the in vivo results.

Another possible explanation could come from the removal of the sidebands owing to modulus processing. As previously mentioned by Serrai et al. [19], the sidebands can increase the standard deviation of the noise and then decrease the SNR obtained with conventional processing. It is worth noting that selecting a region which contains only

noise signal is not so trivial when processing in vivo data. The SNR measured can then vary considerably depending on the spectral region used to calculate the noise standard deviation. In our study, we have tried to select this region in a portion of the spectrum without any visible peaks and/or artifacts and where the hard filter effect is not visible. However, these choices are clearly user-dependent. This is the reason why we have chosen to present in this paper spectra with a large SW. Each reader can then appreciate and compare for himself the SNR obtained by both conventional and modulus techniques.

Another issue, which is not covered here, is the apparent decrease in the linewidth of the metabolites that can be clearly observed on the spectra shown in Figs. 8, 9 and 10. This effect was also mentioned by Serrai et al. [19]. This effect could be partially explained by the removal of the sidebands and also by eddy current correction. This will need to be further investigated. It has also to be noted that, as demonstrated by Serrai in the same publication, the accuracy of metabolites quantification is not affected by modulus processing.

A last issue has to be considered: as modulus processing results in a symmetric spectrum around the water

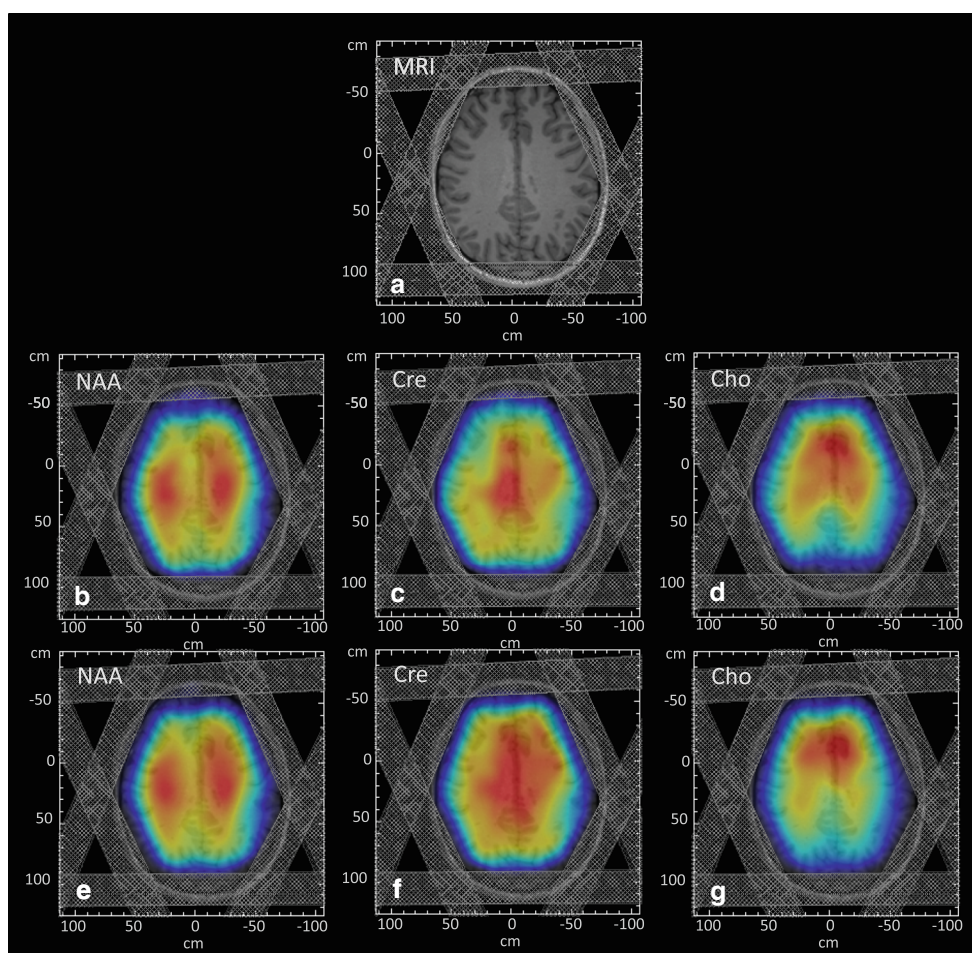


**Fig. 13** Metabolite maps calculated from a CSI acquisition reconstructed using modulus and conventional processing. **a** Shows the conventional MR image used as reference for the CSI experiment (i.e. same field of view, same slice). On **b** the NAA metabolic map is superimposed to the MR image. On **c**, **d** we can see respectively the

creatine and choline metabolic maps. **e–g** Show respectively the NAA, creatine and choline maps obtained using conventional processing. Grid bands shown on the images represent the outer volume saturation used for eliminating the signal of the lipids originating from the skull

resonance, any resonance or artifact that may arise between 5 and 9 ppm (excepting of course the sidebands) will be added to the metabolites region of interest. Consequently, this would definitely corrupt the quantification of the metabolites. Fortunately, this has not been the case in any of our experiments, but if such a problem occurred, these resonances could be removed, before extraction of the modulus, using the HLSVD technique [22] for example.

In this work, we have only shown proton spectroscopy results acquired from the brain. It is clear that the characteristics of brain proton spectra are ideal for the implementation of this method since they include simultaneously a strong water signal and small metabolite signals. The lipids from the skull could create some artifacts, but fortunately the regions where the lipid resonance is at the same level as the water resonance, are usually not of interest. Modulus processing is clearly not applicable to *in vivo* phosphorus spectroscopy because of the absence of

a strong reference signal in these spectra. Nevertheless, the technique may be applicable to muscle proton MR spectroscopy as long as the lipid signal can be suppressed.

Finally, the fact that modulus processing allows the acquisition and processing of non-suppressed water spectra is also in favor of the use of this processing technique. Since the modulus technique allows the acquisition of a non-suppressed water signal, we can take advantage of this additional information in order to optimize the acquisition parameters. Whenever the water signal is required (for absolute quantitation purpose for example), a second experiment is usually performed without water suppression (some groups have developed their own pulse sequences in order to collect the water signal in an interleaved way [2, 15, 27], others have proposed different strategies in order to remove the sidebands [28–32]). This additional experiment can be very time-consuming, like in the case of CSI experiments, since it can last as long as the

water-suppressed experiment itself. Since this additional acquisition can be skipped with modulus processing, the gain in time can be exploited to improve the SNR. For a given acquisition time, when thanks to modulus processing, the total acquisition time is divided by a factor 2, then the SNR is in turn increased by a factor  $\sqrt{2}$ .

It has also to be noted that if the water resonance needs to be quantified in the frequency domain, then this step must be performed before extraction of the modulus of the FID. Otherwise, as detailed in the previous sections, the Rayleigh distributed part of the noise or the contamination induced by a strong lipid resonance would be added to the water peak after fast Fourier transformation.

## Conclusion

We have shown that, whenever a FID contains a signal much higher than the metabolites of interest, working on the modulus of that FID signal allows to correct automatically for the phase and frequency shift of the metabolites, relatively to that signal of reference. In addition, modulus processing presented here also allows to remove the sidebands and phase distortions (due to eddy currents for example).

Despite the decrease in SNR (up to a factor  $\sqrt{2}$ ) predicted by the theory when applying the modulus versus the conventional technique, in practice the SNR measured in vivo is comparable between both processings (the possible reasons for that have been detailed in this paper).

The performance and advantage of modulus processing have been illustrated in three applications: phase coherent averaging, phase alignment of array coils, and  $B_0$  shift correction. In all of these applications, it has been shown that modulus processing is a simple and efficient way to automatically perform phase and frequency shift corrections. Finally, it is important to note that modulus processing offers the advantage to work on non-suppressed water spectra, hence avoiding an additional time-consuming acquisition.

For all these reasons, we think that the modulus correction technique can be a method of choice when analyzing brain proton MR spectroscopy data. Whenever the processing of the spectra cannot be performed manually but absolutely requires to be automated, this is the method of choice for MR spectroscopists.

## References

- Higinbotham J, Marshall I (2000) NMR lineshapes and lineshape fitting procedures. *Annu Rep NMR Spectrosc* 43:59–120
- Thiel T, Czisch M, Elbel GK, Hennig J (2002) Phase coherent averaging in magnetic resonance spectroscopy using interleaved navigator scans: compensation of motion artifacts and magnetic field instabilities. *Magn Reson Med* 47(6):1077–1082
- Dydak U, Weiger M, Pruessmann KP, Meier D, Boesiger P (2001) Sensitivity-encoded spectroscopic imaging. *Magn Reson Med* 46(4):713–722
- Maril N, Lenkinski RE (2005) An automated algorithm for combining multivoxel MRS data acquired with phased-array coils. *J Magn Reson Imaging* 21(3):317–322
- Ratiney H, Sdika M, Coenradie Y, Cavassila S, Ormond D, Graveron-Demilly D (2005) Time-domain semi-parametric estimation based on a metabolite basis set. *NMR Biomed* 18(1):1–13
- Vanhamme L, van den Boogaart A, Van Huffel S (1997) Improved method for accurate and efficient quantification of MRS data with use of prior knowledge. *J Magn Reson* 129(1):35–43
- Brown MA (2004) Time-domain combination of MR spectroscopy data acquired using phased-array coils. *Magn Reson Med* 52(5):1207–1213
- Maudsley AA, Darkazanli A, Alger JR, Hall LO, Schuff N, Studholme C, Yu Y, Ebel A, Frew A, Goldgof D, Gu Y, Pagare R, Rousseau F, Sivasankaran K, Soher BJ, Weber P, Young K, Zhu X (2006) Comprehensive processing, display and analysis for in vivo MR spectroscopic imaging. *NMR Biomed* 19(4):492–503
- Dong Z, Peterson B (2007) The rapid and automatic combination of proton MRSI data using multi-channel coils without water suppression. *Magn Reson Imaging* 25(8):1148–1154
- Natt O, Bezkorovaynyy V, Michaelis T, Frahm J (2005) Use of phased array coils for a determination of absolute metabolite concentrations. *Magn Reson Med* 53(1):3–8
- Prock T, Collins DJ, Dzik-Jurasz AS, Leach MO (2002) An algorithm for the optimum combination of data from arbitrary magnetic resonance phased array probes. *Phys Med Biol* 47(2):N39–N46
- Schaffter T, Bornert P, Leussler C, Carlsen IC, Leibfritz D (1998) Fast 1H spectroscopic imaging using a multi-element head-coil array. *Magn Reson Med* 40(2):185–193
- Antoine JP, Chauvin C, Coron A (2001) Wavelets and related time-frequency techniques in magnetic resonance spectroscopy. *NMR Biomed* 14(4):265–270
- Ebel A, Soher BJ, Maudsley AA (2001) Assessment of 3D proton MR echo-planar spectroscopic imaging using automated spectral analysis. *Magn Reson Med* 46(6):1072–1078
- Bhattacharyya PK, Lowe MJ, Phillips MD (2007) Spectral quality control in motion-corrupted single-voxel J-difference editing scans: an interleaved navigator approach. *Magn Reson Med* 58(4):808–812
- Star-Lack J, Spielman D, Adalsteinsson E, Kurhanewicz J, Terris DJ, Vigneron DB (1998) In vivo lactate editing with simultaneous detection of choline, creatine, NAA, and lipid singlets at 1.5 T using PRESS excitation with applications to the study of brain and head and neck tumors. *J Magn Reson* 133(2):243–254
- Evans CJ, Puts NA, Robson SE, Boy F, McGonigle DJ, Sumner P, Singh KD, Edden RA (2012) Subtraction artifacts and frequency (Mis-)alignment in J-difference GABA editing. *J Magn Reson Imaging*. doi:10.1002/jmri.23923
- Le Fur Y, Nicoli F, Guye M, Confort-Gouny S, Cozzzone PJ, Kober F (2010) Grid-free interactive and automated data processing for MR chemical shift imaging data. *Magn Reson Mater Phy* 23(1):23–30
- Serrai H, Clayton DB, Senhadji L, Zuo C, Lenkinski RE (2002) Localized proton spectroscopy without water suppression: removal of gradient induced frequency modulations by modulus signal selection. *J Magn Reson* 154(1):53–59
- Sijbers J, den Dekker AJ, Van Audekerke J, Verhoye M, Van Dyck D (1998) Estimation of the noise in magnitude MR images. *Magn Reson Imaging* 16(1):87–90

21. Gudbjartsson H, Patz S (1995) The Rician distribution of noisy MRI data. *Magn Reson Med* 34(6):910–914
22. Pijnappel W, Van den Boogaart A, De Beer R, Van Ormondt D (1992) SVD-based quantification of magnetic resonance signals. *J Magn Reson* 97:97–122
23. Sdika M, Le Fur Y, Cozzone PJ (2011) Optimal recombination of multi-coils CSI data using image based sensitivity map. In: *Proceeding of the 19th annual meeting, international society of magnetic resonance in medicine*, Montreal, Canada, p 3478
24. Sdika M, Le Fur Y, Cozzone PJ (2011) Optimal recombination of multi-coils CSI data using image based sensitivity map. In: *Proceedings of the European Society of magnetic resonance in medicine and biology*, Leipzig, DE, p 583
25. Maudsley AA, Domenig C, Govind V, Darkazanli A, Studholme C, Arheart K, Bloomer C (2009) Mapping of brain metabolite distributions by volumetric proton MR spectroscopic imaging (MRSI). *Magn Reson Med* 61(3):548–559
26. Klose U (1990) In vivo proton spectroscopy in presence of eddy currents. *Magn Reson Med* 14(1):26–30
27. Ebel A, Maudsley AA (2005) Detection and correction of frequency instabilities for volumetric 1H echo-planar spectroscopic imaging. *Magn Reson Med* 53(2):465–469
28. Chadzynski GL, Klose U (2013) Proton CSI without solvent suppression with strongly reduced field gradient related sideband artifacts. *Magn Reson Mater Phy* 26(2):183–192
29. Chadzynski GL, Klose U (2010) Chemical shift imaging without water suppression at 3 T. *Magn Reson Imaging* 28(5):669–675
30. Dong Z, Dreher W, Leibfritz D (2004) Experimental method to eliminate frequency modulation sidebands in localized in vivo 1H MR spectra acquired without water suppression. *Magn Reson Med* 51(3):602–606
31. Dong Z, Dreher W, Leibfritz D (2006) Toward quantitative short-echo-time in vivo proton MR spectroscopy without water suppression. *Magn Reson Med* 55(6):1441–1446
32. Nixon TW, McIntyre S, Rothman DL, de Graaf RA (2008) Compensation of gradient-induced magnetic field perturbations. *J Magn Reson* 192(2):209–217